



# Uncooperative Spacecraft Pose Estimation Using an Infrared Camera During Proximity Operations

Jian-Feng Shi,<sup>\*</sup> Steve Ulrich<sup>†</sup>

*Carleton University, Ottawa, Ontario K1S 5B6, Canada*

Stephane Ruel,<sup>‡</sup> Martin Ancil<sup>§</sup>

*Neptec Design Group Ltd., Kanata, Ontario K2K 1Y5, Canada*

This paper presents the design of a pose estimation method for autonomous robotic proximity operations with an uncooperative target using a single infrared camera and a simple three-dimensional model of the target. Specifically, the presented method makes use of the so-called SoftPOSIT algorithm to solve the model-to-image registration problem. This particular method is found to be most useful for ranges where surface features are not well resolved, that is, from approximately 30 to 500 meters. The proposed solution is validated in preliminary numerical simulations using low-resolution CAD models of Envisat and ISS that emulate IR images, and obtained results are reported and discussed.

## I. Introduction

AUTONOMOUS proximity operations are widely recognized as an important technological capability that enables various spacecraft missions, such as rendezvous and docking, re-supply, on-orbit servicing, inspection, orbital debris removal, and space structure assembly.<sup>1</sup> Over the last few decades, autonomous proximity operations have been demonstrated in space for International Space Station (ISS) re-supply missions through the Russian Progress and Soyuz, the Japanese H-II Transfer Vehicle, and the European Automated Transfer Vehicle (ATV) cargo spacecraft. More recently, SpaceX's Dragon and Orbital Sciences' Cygnus spacecraft have also completed rendezvous and docking maneuvers with the ISS. Other notable experimental missions validating proximity operation technologies include JAXA's ETS-VII<sup>2</sup> and Boeing's Orbital Express (OE). Unfortunately, the aforementioned missions dealt with a cooperative target, i.e., spacecraft equipped with known fiducial markers. This greatly facilitated real-time pose estimation process; one of the key enabling technologies for autonomous proximity operations that determines the relative states between the chaser and the target vehicles. For example, OE advanced video guidance sensor (AVGS) used photogrammetric algorithms to determine the six-degrees-of-freedom pose, i.e., the three-dimensional relative position and orientation between both vehicles. Laser diodes were also used to illuminate retro-reflective markers installed on the target spacecraft, to filter other light frequencies, making it more immune to varying lighting conditions.<sup>3</sup> Soon after the success of OE, the ATV completed its first automated rendezvous and docking maneuver with ISS.<sup>4</sup> At far range, the ATV determined its relative position through GPS receivers on both the ATV and the ISS, and in close range it used videometers that bounced pulsed laser beams off of passive retro-reflectors, and image pattern analysis to estimate its relative pose.<sup>5</sup>

However, when the target spacecraft is not equipped with known markers, such cooperative pose estimation systems cannot be employed, and more advanced pose estimation technologies are required. Pose estimation systems for uncooperative proximity operations, such as those relying solely on optical stereo sensors, are currently an active area of research. Indeed, visual-based systems offer several advantages, such as low power, mass and volume requirements.<sup>6</sup> Building upon the U.S. Naval Research Laboratory's Low

<sup>\*</sup>PhD Student, Department of Mechanical and Aerospace Engineering, 1125 Colonel By Drive. Member AIAA.

<sup>†</sup>Assistant Professor, Department of Mechanical and Aerospace Engineering, 1125 Colonel By Drive. Senior Member AIAA.

<sup>‡</sup>Director, Exploration Technology Programs, 302 Legget Drive.

<sup>§</sup>Senior Software Specialist, 302 Legget Drive.

Impact Inspection Vehicle program,<sup>7,8</sup> the Massachusetts Institute of Technology (MIT) Space Systems Laboratory recently developed the Visual Estimation for Relative Tracking and Inspection of Generic Objects (VERTIGO) experimental facility.<sup>9</sup> Consisting of a software/hardware upgrade to the existing Synchronized, Position Hold, Engage, Reorient, Experimental Satellites (SPHERES) ISS facility, VERTIGO enables research and development of uncooperative optical-based relative navigation and mapping techniques capable of achieving two main objectives: (1) performing a fly-around maneuver by relying solely on optical stereo monochrome camera hardware and gyroscopes, and (2) building a three-dimensional model of a uncooperative object while simultaneously estimating the relative position, attitude, linear and angular velocities as well as its centre of mass, principal axes of inertia and ratios of principal moments of inertia through a simultaneous localization and mapping (SLAM) technique. In 2013 and 2014, these techniques were validated with the SPHERES free-flyer nanosatellites maneuvering in a six degrees-of-freedom microgravity environment, inside the ISS Japanese Experiment Module.<sup>10-13</sup> While the fly-around stereo camera system was simple enough to be executed in real-time, the SLAM-based technique, due to its high computational complexity, did not allow real-time operations (it required approximately 10 minutes to obtain a solution on a 1.2 GHz x86 embedded computer). Also, while visual cameras are suitable sensors to solve the uncooperative pose estimation problem, they are nevertheless susceptible to varying and harsh orbital lighting conditions and camera calibration errors.

To overcome the inherent lighting condition and calibration problems of optical stereo cameras, Neptec's TriDAR system uses a three-dimensional laser sensor, and a thermal infrared imager.<sup>14</sup> Considered as the current state-of-the-art pose estimation technology for uncooperative missions, the TriDAR system uses preliminary knowledge about the target spacecraft through an on-board three-dimensional model to provide six degree-of-freedom relative pose information in real time. The algorithms were optimized to use only 100 sparse points from the laser sensor in an undisclosed variant of the so-called Iterative Closest Point (ICP) algorithm.<sup>15</sup> Space Shuttle tests on STS-128, STS-131 and STS-135 missions to the ISS demonstrated a high pose estimation accuracy achieved by the TriDAR system.<sup>14</sup> During these missions, the thermal imager was used to provide range and bearing information for far-range rendezvous operations. One drawback with TriDAR is its relatively high power and mass requirements. While this is acceptable for larger ISS cargo-resupply spacecraft, e.g., SpaceX Dragon, and Orbital Sciences Cygnus, this drawback could rule out the use of this sensor for smaller spacecraft missions, where available power and mass is highly limited.

In this context, this paper presents the design of an uncooperative pose estimation system that uses a single thermal infrared camera and an approximate three-dimensional geometrical representation of the target spacecraft. The proposed design uses an iterative algorithm that minimizes a global cost function at each iteration step, to solve the *model-to-image registration problem* (also known as the *simultaneous pose and correspondence problem*), which is defined as the determination of the 6-degrees-of-freedom pose given a model of the object consisting of three-dimensional reference points and a single two-dimensional image of these points.<sup>16</sup> Note that three correspondences between object and image points is the minimum necessary to constrain the object to a finite number of poses. Over the years, many solutions that specifically make use of alignment techniques have been derived to solve the correspondence problem, which often result in the use of geometrical, probabilistic, and iterative schemes. For example, Haralik et al.<sup>17</sup> determined a wire frame object position relative to the camera by using cones to transform a two-dimensional (2D) to a three-dimensional (3D) matching problem to a 3D to 3D matching problem. Lowe<sup>18</sup> used probabilistic ranking of invariant structures to search for matches and use spatial correspondence to match 3D models. Pinjo<sup>19</sup>



Figure 1. TriDAR installed on Orbital Sciences Cygnus spacecraft. Courtesy of Neptec Design Group Ltd.

used 3D moment tensors to determine proper transformations relating two different orientations. Thompson and Mundy<sup>20</sup> defined a vertex-pair to determine affine transformation between a 3D model and a 2D image using a clustering approach. Gavrilu and Groen<sup>21</sup> used a technique called Geometric Hashing to identify an object in the scene by indexing invariant features of the model in a hash table, which is robust to up to 50% occlusion. Grimson and Huttenlocher<sup>22</sup> derived a matching condition based on a statistical occupancy model, and provides a method for setting threshold so the probability of a random match is minimized. Jurie<sup>23</sup> used a Gaussian distribution to model image noise in order to improve the probability of matching, and he further used a recursive multi-resolution exploration of the pose space for object matching. More recently, David et al.<sup>24,25</sup> developed the Simultaneous Pose and Correspondence Determination algorithm, referred to as SoftPOSIT, which will be employed as the centerpiece of the uncooperative pose estimation system developed in this work.

## II. Model-to-image Registration

This section first formally defines the reference frames, or coordinate systems, used in this work. Then, it describes SoftPOSIT, which represents the core model-to-image registration technique used in the proposed uncooperative pose estimation system.

The approach used in this study can be broken down into two main steps: (1) application of image processing techniques, and (2) iterative pose estimation. This approach is a combination of a number of existing techniques. Step 1 includes region segmentation and edge detection/line thinning for robust point feature extractions. These point features are required for the task of model-based object recognition and pose estimation in Step 2. Due to its ease of implementation and robustness, the pose estimation algorithm used in this paper corresponds to the *SoftPOSIT* algorithm<sup>24,25</sup> which integrates an iterative pose technique called *POSIT* (Pose from Orthography and Scaling with Iterations),<sup>26</sup> and an iterative correspondence assignment technique called *softassign*<sup>27</sup> into a single iteration loop. A global cost function is defined that captures the nature of the problem in terms of both pose and correspondence and combines the formalisms of both iterative techniques. The correspondence and the pose are determined simultaneously by applying a deterministic annealing schedule and by minimizing this global cost function at each iteration step.

This section first formally defines the reference frames, or coordinate systems, used in this work and second describes SoftPOSIT, which represents the core model-to-image registration technique used in the proposed uncooperative pose estimation system.

### II.A. Coordinate System Definition

The spacecraft coordinate systems for two spacecraft relative to an inertial coordinate system located at the centre of the Earth  $\mathcal{F}_{LS}$  are defined in order to compute the relative position and orientation between the two vehicles.  $\mathcal{F}_{CO}$  and  $\mathcal{F}_{SO}$  describe the target client and servicing spacecraft (SS) orbit Local Vertical Local Horizontal (LVLH) coordinate system respectively. Where  $x$  is in the direction of orbit motion,  $z$  is in the direction of the inertial coordinate origin and  $y$  completes the right hand.  $\mathcal{F}_{CS}$  and  $\mathcal{F}_{SS}$  coordinate frames describe the client and servicer spacecraft mechanical structural coordinate system respectively. The structural coordinate system is fix the the spacecraft body located at mechanical coordinate of convenience.  $\mathcal{F}_{CB}$  and  $\mathcal{F}_{SB}$  describe the client satellite (CS) and SS Centre of Mass (COM) frame of reference respectively. The body coordinates are positioned at the vehicle mass center and is fixed to the spacecraft. It has the same orientation as the spacecraft mechanical structural coordinate system. Finally, the camera coordinate system  $\mathcal{F}_{VW}$  is located at the center of the camera lens on the SS, the camera has its  $z$  axis pointed out from the boresight of the camera, with  $y$  axis pointed vertically down across the camera and the  $x$  axis making the right hand. The 2-dimensional camera image frame  $\mathcal{F}_{ia}$  is centered in the image with  $x$  and  $y$  parallel to  $\mathcal{F}_{VW}$ . Fig. 2 shows the various coordinate systems considered.

### II.B. SoftPOSIT

Consider the camera view of the CS with  $M$  points fixed to the body denoted by  $PW_k$  where  $k = 1, \dots, M$  is the number of point in the sequence. These points are the corner vertices of the CS body and are expressed in the  $\mathcal{F}_{CS}$  frame. Fig. 3 shows the various camera coordinate systems considered.  $PW_k$  can be translated to be expressed in the  $\mathcal{F}_{CB}$  frame when given the COM position relative to  $\mathcal{F}_{CS}$ . When viewed from the SS camera,  $PW_k$ 's image is denoted by  $pi_k$ . The position of  $PW_k$  relative to  $\mathcal{F}_{VW}$  expressed in  $\mathcal{F}_{VW}$  and

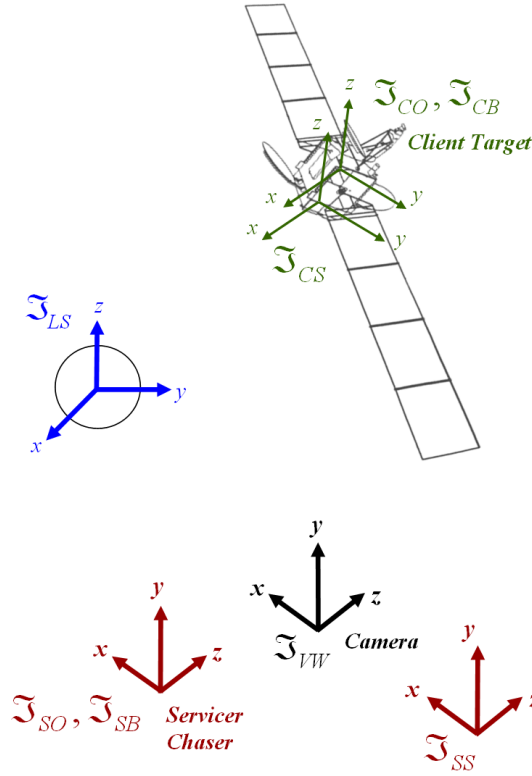


Figure 2. Coordinate system definition.

$pi_k$ 's position in  $\mathcal{F}_{ia}$  is denoted by  $\mathbf{r}_{VW}^{VW, PW_k}$  and  $\mathbf{r}_{ia}^{ia, pi_k}$  respectively and their relationships to the position and orientation of the CS body frame can be found in Eq. (1) and Eq. (2) respectively.

$$\mathbf{r}_{VW}^{VW, PW_k} = \mathbf{r}_{VW}^{VW, CB} + \mathbf{R}^{VW, CB} \mathbf{r}_{CB}^{CB, PW_k} \quad (1)$$

$$\mathbf{r}_{ia}^{ia, pi_k} = s(f) \begin{bmatrix} 1 & 0 & 0 \\ 0 & 1 & 0 \end{bmatrix} \mathbf{r}_{VW}^{VW, PW_k} \quad (2)$$

where  $s$  is a scaling ratio between the focal length and the  $z$  distance from the camera to the CS COM expressed in the camera frame as defined in Eq. (3).

$$s = \frac{f}{\mathbf{r}_{zVW}^{VW, CB}} \quad (3)$$

Suppose the initial position and orientation estimation of the CS body differs from the actual CS and the projection of the CS on-board model. The projection of  $PW_k$  on to the image plane ( $I_1$ ) will differ from the actual camera image as shown in Fig. 4. The POSIT method suggests to project the physical world point on to a plane ( $I_2$ ) that is parallel with the CS body frame  $\mathcal{F}_{CB}$ . Let  $w_k$  be a ratio between the  $z$  position of  $PW_k$  and  $CB$  per Eq. (4)

$$w_k = \frac{r_{zVW}^{VW, PW_k}}{r_{zVW}^{VW, CB}} \quad (4)$$

then by inspection of the two separate similar triangles  $\angle(\mathcal{F}_{I3}, \mathcal{F}_{VW}, PW_{kActual})$  and  $\angle(\mathcal{F}_{I2}, \mathcal{F}_{VW}, PW_{kProjected})$ , it can be shown  $w_k$  can also be expressed as Eq. (5).

$$w_k = \frac{\|\mathbf{r}_{ia}^{ia, pi_{k2}}\|}{\|\mathbf{r}_{ia}^{ia, pi_k}\|} \quad (5)$$



Eq. (5) allows the computation of  $\|\mathbf{r}_{ia}^{ia,pi_k2}\|$ . The other component that is required for the *softassign* process is the projected image of the on-board model. To compute this, the rotation matrix rotating a vector expressed in the CS body frame to the SS camera frame is represented as Eq. (6)

$$\mathbf{R}^{VW,CB} = \begin{bmatrix} \mathbf{R}_x^{VW,CB} \\ \mathbf{R}_y^{VW,CB} \\ \mathbf{R}_z^{VW,CB} \end{bmatrix} \quad (6)$$

where  $\mathbf{R}_x^{VW,CB}$ ,  $\mathbf{R}_y^{VW,CB}$ , and  $\mathbf{R}_z^{VW,CB}$  are row vectors of the  $\mathbf{R}^{VW,CB}$  matrix. It should also be noted that these are the unit vectors of the camera coordinate system ( $\mathcal{F}_{VW}$ ) expressed in the CS body frame ( $\mathcal{F}_{CB}$ ). Using the unit vectors of Eq. (6), the on-board model's image projection on to the image plane  $I_1$  can be computed by Eq. (7)

$$\begin{aligned} \mathbf{r}_{ia}^{ia,pi_k} &= \begin{bmatrix} x_k \\ y_k \end{bmatrix} \\ &= s(f) \begin{bmatrix} \mathbf{R}_x^{VW,CB} \mathbf{r}_{CB}^{CB,PW_k} + \mathbf{r}_{xVW}^{VW,CB} \\ \mathbf{R}_y^{VW,CB} \mathbf{r}_{CB}^{CB,PW_k} + \mathbf{r}_{yVW}^{VW,CB} \end{bmatrix} \end{aligned} \quad (7)$$

Eq. (7) can be re-formulated using  $\mathbf{Q}$  and  $\mathbf{P}$  matrices as defined by Eq. (8) and Eq. (9) respectively.

$$\mathbf{Q}_x = s(f) \begin{bmatrix} \mathbf{R}_x^{VW,CB} \\ \mathbf{r}_{xVW}^{VW,CB} \end{bmatrix} \quad (8)$$

$$\mathbf{Q}_y = s(f) \begin{bmatrix} \mathbf{R}_y^{VW,CB} \\ \mathbf{r}_{yVW}^{VW,CB} \end{bmatrix}$$

$$\mathbf{P}_k = \begin{bmatrix} \mathbf{r}_{CB}^{CB,PW_k} \\ 1 \end{bmatrix} \quad (9)$$

Finally, the distance between the model projected image and the actual image can be computed by Eq. (10).

$$\begin{aligned} d_k &= \sqrt{(\mathbf{Q}_x \cdot \mathbf{P}_k - w_k x_k)^2 + (\mathbf{Q}_y \cdot \mathbf{P}_k - w_k y_k)^2} \\ &= |p_{i_k Model} p_{i_k 2}| \\ &= s(f) |PW_{k Model} PW_{k Actual}| \end{aligned} \quad (10)$$

As a side note, Eq. (10) also shows the physical distance between the estimated model and the actual spacecraft is a scaled multiple of the difference in image distance  $d_k$ . Once  $d_k$  is known, a *Global Objective Function*  $E$  can be computed to sum over square of the image distance per Eq. (11).

$$\mathbf{E} = \sum_{k=1}^M d_k^2 \quad (11)$$

The minimum distance that would result in the model coinciding with the actual CS is the partial derivative of the *Global Objective Function* with respect to the  $\mathbf{Q}$  matrix per Eq. (12).

$$\begin{aligned} \frac{\partial E}{\partial \mathbf{Q}_x} &= \mathbf{0} \\ \frac{\partial E}{\partial \mathbf{Q}_y} &= \mathbf{0} \end{aligned} \quad (12)$$

The solution of Eq. (12) is given by Eq. (13) and Eq. (14), which will allow best estimation of the CS position and orientation that is optimally matched with the real image and real world spacecraft position and orientation.

$$\mathbf{L} = \sum_{k=1}^M \mathbf{P}_k \mathbf{P}_k^T \quad (13)$$

$$\begin{aligned}\mathbf{Q}_x &= \mathbf{L}^{-1} \sum_{k=1}^M w_k x_k \mathbf{P}_k \\ \mathbf{Q}_y &= \mathbf{L}^{-1} \sum_{k=1}^M w_k y_k \mathbf{P}_k\end{aligned}\tag{14}$$

For number of image points differ from the on-board model vertices, Eq. (10) to Eq. (14) are modified to include an additional index  $j$  that can range between  $j = 1, \dots, N$  number of image points. The general equation for computing  $\mathbf{Q}$  is provided by Eq. (15) to Eq. (18) respectively. An example of the multiple image and model points scene is depicted by Fig. 5.

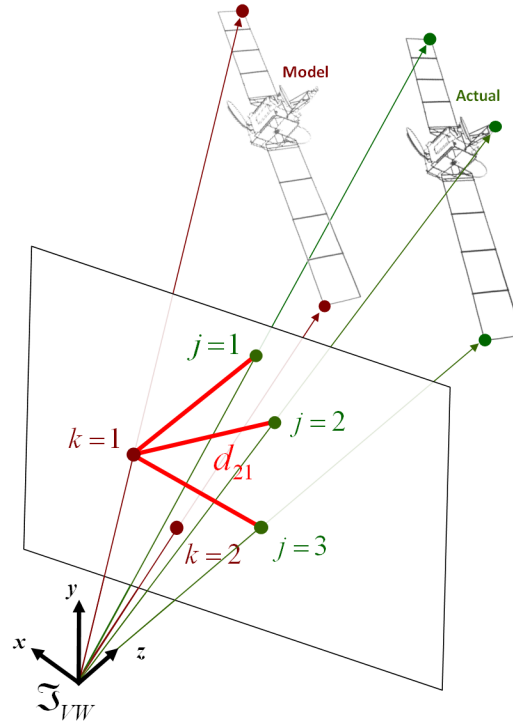


Figure 5. Multiple image and model point example.

$$\begin{aligned}d_{jk} &= \sqrt{(\mathbf{Q}_x \cdot \mathbf{P}_k - w_k x_j)^2 + (\mathbf{Q}_y \cdot \mathbf{P}_k - w_k y_j)^2} \\ j &= 1, \dots, N \\ k &= 1, \dots, M\end{aligned}\tag{15}$$

where,

$$\mathbf{E} = \sum_{j=1}^N \sum_{k=1}^M m_{jk} (d_{jk}^2 - \alpha)\tag{16}$$

$$\mathbf{L} = \sum_{j=1}^N \sum_{k=1}^M m_{jk} \mathbf{P}_k \mathbf{P}_k^T\tag{17}$$

$$\begin{aligned}\mathbf{Q}_x &= \mathbf{L}^{-1} \sum_{j=1}^N \sum_{k=1}^M m_{jk} w_k x_j \mathbf{P}_k \\ \mathbf{Q}_y &= \mathbf{L}^{-1} \sum_{j=1}^N \sum_{k=1}^M m_{jk} w_k y_j \mathbf{P}_k\end{aligned}\tag{18}$$



For the general case, a weighting correspondence variable  $m_{jk}$  is introduced.  $m_{jk}$  satisfy a number of correspondence constraints. A term  $\alpha$  is introduced to allow the iterative minimization of the *Global Objective Function*. To do this, two main iteration loops based on the *softassign* method by Gold<sup>27</sup> are used

1. Compute the correspondence weight  $m_{jk}$ . Using Sinkhorn's method<sup>28</sup> for loop iteration, this is where each row and column of the correspondence matrix is normalized by the sum of the elements of that row or column, the resulting matrix has positive elements with all rows and columns summing to 1. The correspondence calculation for each loop is calculated per Eq. (19).
2. The outer iteration loop is known as the deterministic annealing process. This process computes kinematics i.e. to determine  $\mathbf{Q}_x$  and  $\mathbf{Q}_y$ , and to compute  $w_k$ . To begin the annealing process, the correspondence variable is initialized to Eq. (20). Where  $\gamma$  is some scaling factor and  $\beta$  increases on every iteration until it reaches an upper limit or if the pose modification has converged based on some tolerance.

$$m_{jk}^{i+1} = \frac{m_{jk}^i}{\sum_{k=1}^{M+1} m_{jk}^i} \quad 1 \leq j \leq N, \quad 1 \leq k \leq (M+1) \quad (19)$$

$$m_{jk}^{i+1} = \frac{m_{jk}^{i+1}}{\sum_{k=1}^{N+1} m_{jk}^{i+1}} \quad 1 \leq j \leq (N+1), \quad 1 \leq k \leq M$$

$$m_{jk}^0 = \gamma \exp(-\beta(d_{jk}^2 - \alpha)) \quad (20)$$

### III. Pose Estimation System

The uncooperative pose estimation system is provided in Fig. 6. As shown in this figure, the system takes as input infrared camera images. However, for preliminary testing of the developed system, simulated images based on low-resolution CAD models are used to emulate camera images. Note that these low-resolution CAD models are also used to generate the on-board point models that SoftPOSIT requires. Two examples of such spacecraft CAD models were developed in this work, these are: Envisat and ISS, as shown in Fig. 7. The low-resolution CAD model dimensions were used to generate an on-board model for the pose determination software. More details on the on-board model generation is provided in the following section.

In addition to the on-board point model generation, upon initialization, the software performs an internal calibration based on some saved images that will allow the software to determine the scaling between the Cartesian space and pixel coordinates. The on-board point model generation and calibration is ran during the initialization process or whenever the user makes the initialization request. In the main pose estimation algorithm, three main components are used in determining the final position and orientation of the CS. These components are:

1. image processing,
2. SoftPOSIT, and
3. coordinate kinematics.

The image processing phase computation involves cleaning, refining the input image, developing outline of the image, and corner detect the image. This combination was found to have the best effect in finding the boundary corner vertices. The image processing phase will be discussed in detail in the following section.

Once the image is processed, a list of coordinate is computed from the corner detected image pixels. These image coordinates are passed into the SoftPOSIT algorithm along with the on-board model point coordinates.

The SoftPOSIT point coordinates are provided from the Point Model Generation block. Based on the position and orientation of the CS body, the on-board model point sets is further culled to remove the hidden points that can not be imaged. The point culling procedure will be discussed in detail in the following section. Once the image coordinates and on-board model coordinates are received by SoftPOSIT, it performs an initialization and begins the deterministic annealing process and Sinkhorn's iteration as previously described. The final output of the SoftPOSIT algorithm provides a position of the CS body



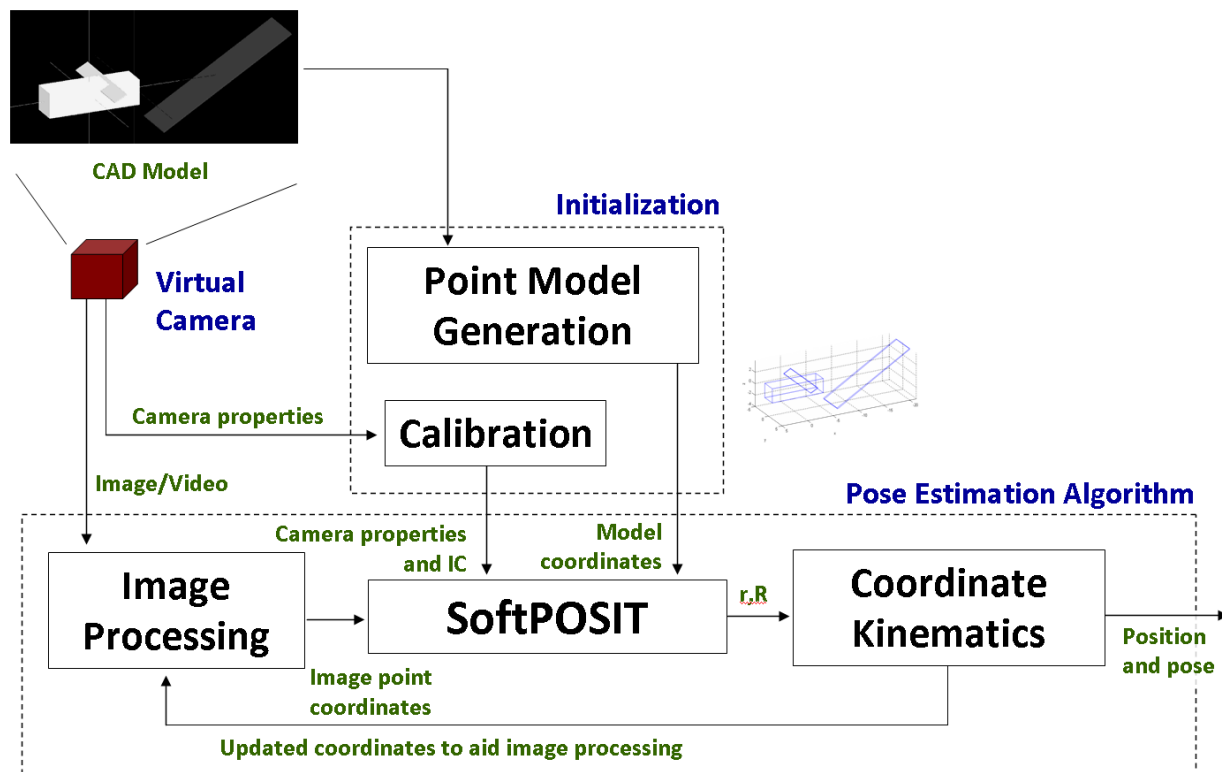


Figure 6. Spacecraft pose estimation software architecture.

relative to the camera expressed in the camera frame and the rotation from the CS body frame to the camera frame.

Once the CS body frame position and orientation is known, it is passed into the third and final phase of the algorithm for the kinematic coordinate calculation in to position and pose of the CS relative to the LVLH orbit frame as well as relative to the SS body frame. The coordinate kinematics calculation block can also provide updated coordinates to aid the image processing effort.

### III.A. On-board Model Generation

A coordinate generation algorithm was developed to convert basic solids such as rectangle, cone, ellipse and cylinder (shown in Fig. 8) and build them into higher order spacecraft. Examples of the higher order spacecraft built from basic solids are provided in Fig. 9. The generic routine takes the basic length, width, height or diameter information in combination with the local body coordinate relative to the spacecraft structural frame and generate an on-board model consists of a matrix of Cartesian coordinates. These Cartesian coordinate represent the vertices on the on-board model. In the case of cylinder or ellipse, the rounded surfaces are approximated by straight sides. The number of points for the round shape is entered as input. Another matrix that is generated as part of the Point Model Generation process is the adjacent matrix. The adjacent matrix describes how each vertices is connected to another and is of the order of the number of points in the on-board model. Without any connections, the adjacent matrix is identity. For example, if the on-board model coordinate 1 is connected to coordinate 2, then the adjacent matrix value for row 1 column 2 is set to 1. If there is no connection, the adjacent matrix value is set to 0. Since coordinate 2 is also connected with coordinate 1, the adjacent matrix is a symmetrical.

### III.B. Image Processing

An eight bit 640x480 graymap image is supplied by a 43 mm lens and 40 degree field of view virtual 3D model camera. The image is edge detected using the Roberts Cross method using threshold of 0.1.<sup>29</sup> Based

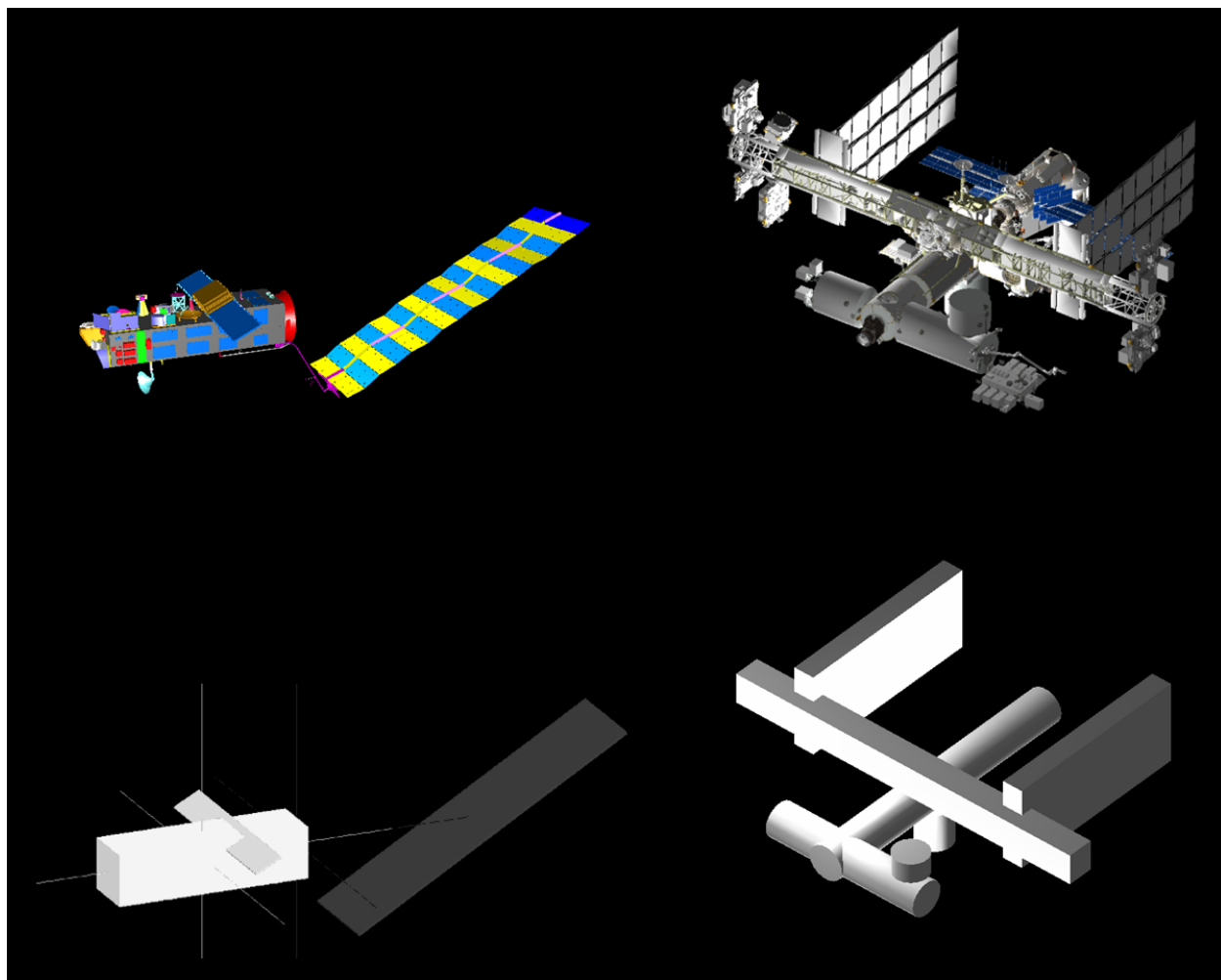


Figure 7. CAD models. Top row: high-resolution CAD models based on which the low-resolution models were created. Bottom row: low-resolution CAD models used to emulate camera images and to generate the on-board point models. Left column: Envisat models. Right column: ISS models.

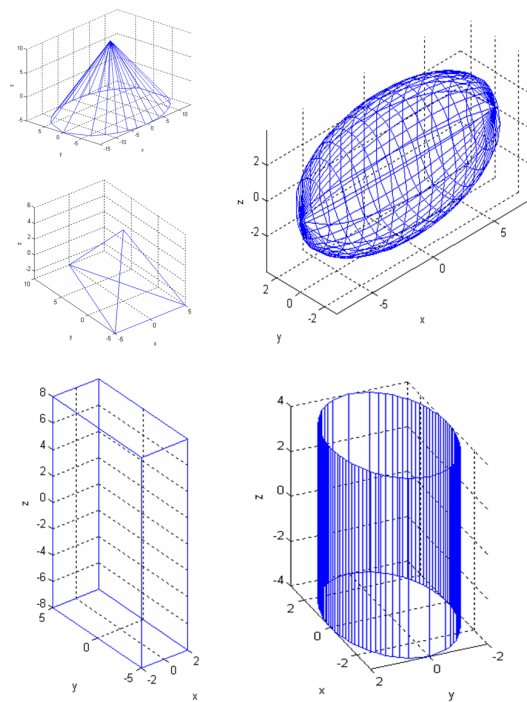


Figure 8. Elemental building shapes.

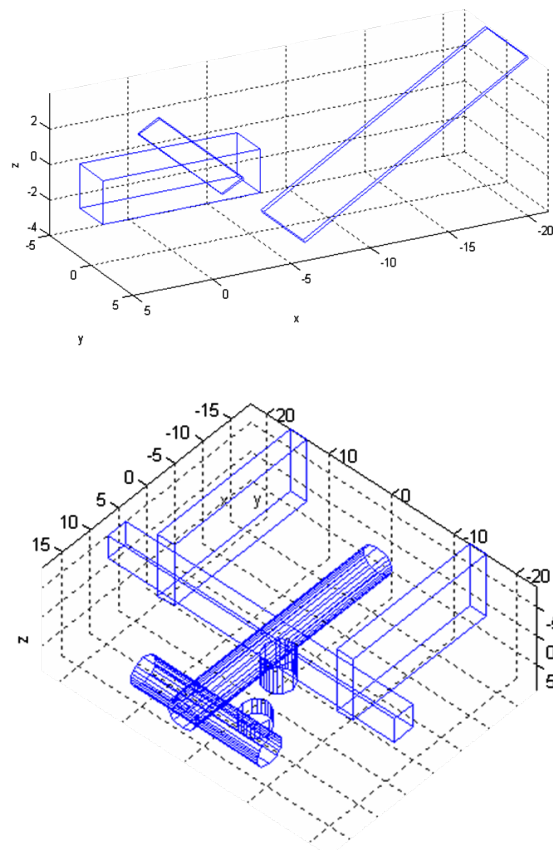


Figure 9. On-board models. Top: Envisat. Bottom: ISS.

on experiments, the Roberts method produces less edges than the Canny's method,<sup>30</sup> but takes roughly half the time to process. Once outer edges are detected, image points are generated using Harris corner detector on the edge image. The last procedure is for the software to convert the image points into pixel coordinates. Fig. 10 shows the results of the image processing, the CAD grayscale image is used to simulate the infrared camera image input for Envisat and ISS simplified 3D models (upper and lower left respectively). This is then edge detected and corner detected using Roberts Cross and Harris corner detection method respectively (upper and lower right).

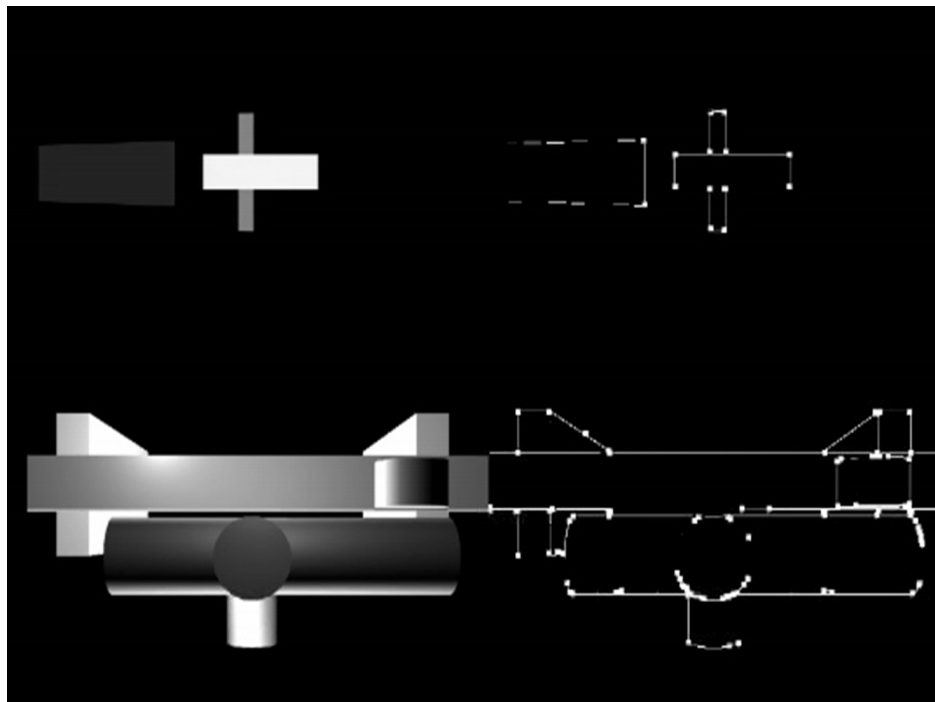


Figure 10. Pre and post processed image. Top left: Simplified Envisat CAD model image. Top right: Envisat Edge and Corner detection. Bottom left: Simplified ISS CAD model image. Bottom right: ISS Edge and Corner detection.

## IV. Simulation Results

In this section, the SoftPOSIT algorithm is tested on some basic geometries then used against full spacecraft models such as Envisat and the ISS.

### IV.A. Simple Cylinder Pose Estimation

Once implemented, the SoftPOSIT algorithm was tested against several basic shapes. The deterministic annealing iterations for a cylinder body is shown in Fig. 11. The red dotted lines represent the camera image, and the blue dotted line and lines represent the on-board model. The initial state is presented in the upper most left image, The Six subsequent iteration steps are displayed to show the progress of the SoftPOSIT algorithm. At each iteration, the on-board model is pushed towards the final image until finally it is coincide with the image. It should be noted that the image points were deliberately degraded so it does not have the perspective points of the cylinder back end. Without the perspective backend, there are multiple solutions SoftPOSIT can take in wobble, since the backend points are not fixed. Furthermore, when encountering a shape that is symmetrical about one or both axis, the SoftPOSIT algorithm cannot distinguish between points from either side of the axis. This is particularly demonstrated in the boresight axis in the cylinder example, where any boresight angle is a solution if there is no identification marking on the cylinder boresight face itself. The symmetrical ambiguity is alleviated if the a-priori state of the object is known to some degree. This allows an initial estimate that is close to the true object position and orientation and therefore the solution would converge towards the true position and orientation. A cube example is demonstrated in Fig. 12. In the first test, the target cube position and orientation with respect

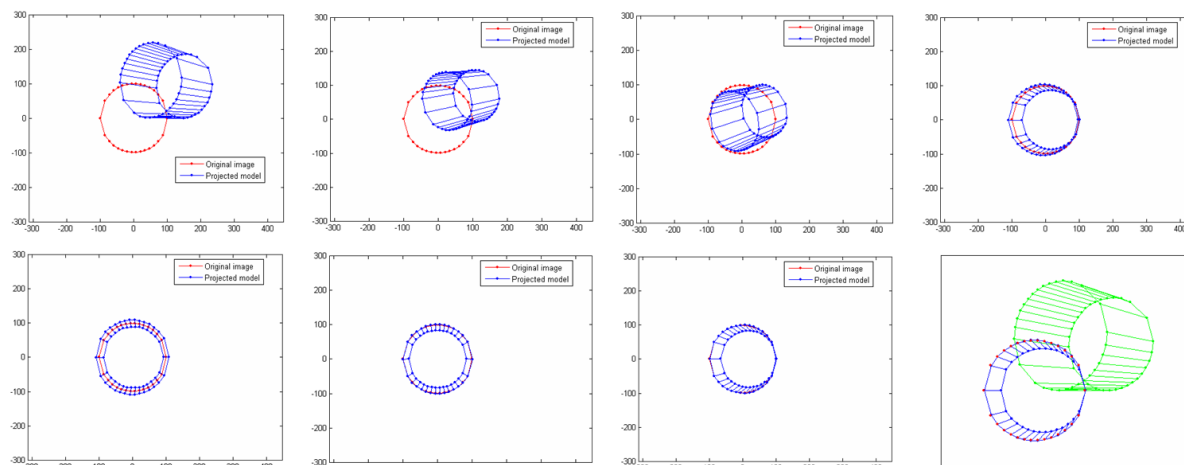


Figure 11. Matching a cylinder image using SoftPOSIT.

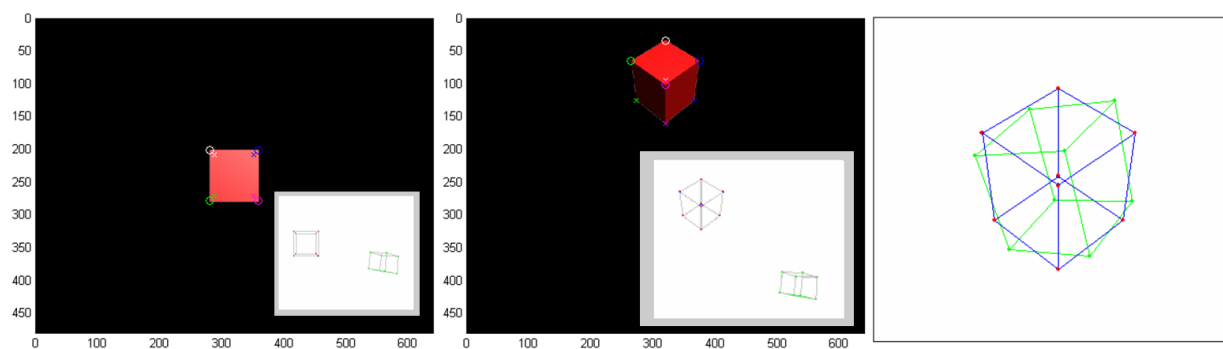


Figure 12. Matching a cube image using SoftPOSIT.

to the camera is set to  $[0;0;5]$  meters and  $[0;0;0]$  degrees respectively. An error of 15 degrees was applied to all axis in the on-board model to start the SoftPOSIT process. The left figure shows SoftPOSIT translate from the initial (green) position to the final (red) position by the end of the annealing process. A second test (centre and right figure) starts with cube position of  $[0;-2;5]$  meters and  $[135;-90;30]$  degrees<sup>a</sup>, similar to test 1, an error of 15 degrees was applied to all axis in the on-board model. SoftPOSIT once again find the final position and orientation. The final position and orientation error from the target is  $[0.004;-0.001;-0.022]$  meters and  $[-0.163;-0.134;0.109]$  degrees. It should be noted that the picture resolution in this test is  $640 \times 480$  pixels, and image detection of the corner points is the exact case. The accuracy of the SoftPOSIT is proportional to the pixel density in the image. Both tests demonstrate the SoftPOSIT software can deliver good position and orientation estimation base only on 2D images of the target object.

#### IV.B. Envisat Pose Estimation

An example of a mission that would benefit from the infrared-based pose estimation system is the disposal of European Space Agency's (ESA) Environmental Satellite (Envisat). Envisat was launched on March 1, 2002 and ended on April 8, 2012 due to an unexpected loss of contact. Due to the satellite's significant size and location of a highly populated sun-synchronous polar orbit of 796 km with inclination of 98.54 degrees, it is deemed to be a high-risk space debris, as a collision with Envisat would result in significant numbers of sub-debris in Low Earth Orbit. Recently, Kurcharski et al.<sup>31</sup> investigated the spin rate of Envisat, and determined it to be 1.33 deg/s counter clock-wise about an axis that is 62 deg from nadir. A simulated Envisat via a Computer Aided Design (CAD) program is provided in Fig. 7. This shall be used as the baseline model to test the pose estimation algorithm developed in this work.

Fig. 13 shows the initial position of the Envisat in blue on the right side figure at  $[3;3;3]$  meters and  $[30;30;30]$  degrees, the final position is in red plot in the same figure at  $[0;0;50]$  meters  $[0;0;0]$  degrees. The final error is  $[0.008;0.034;0.326]$  meters and  $[0.749;0.001;-0.144]$  degrees. Similar to the cube example, the image detection of the corner points is the exact case. Fig. 14 shows the SoftPOSIT calculation for a

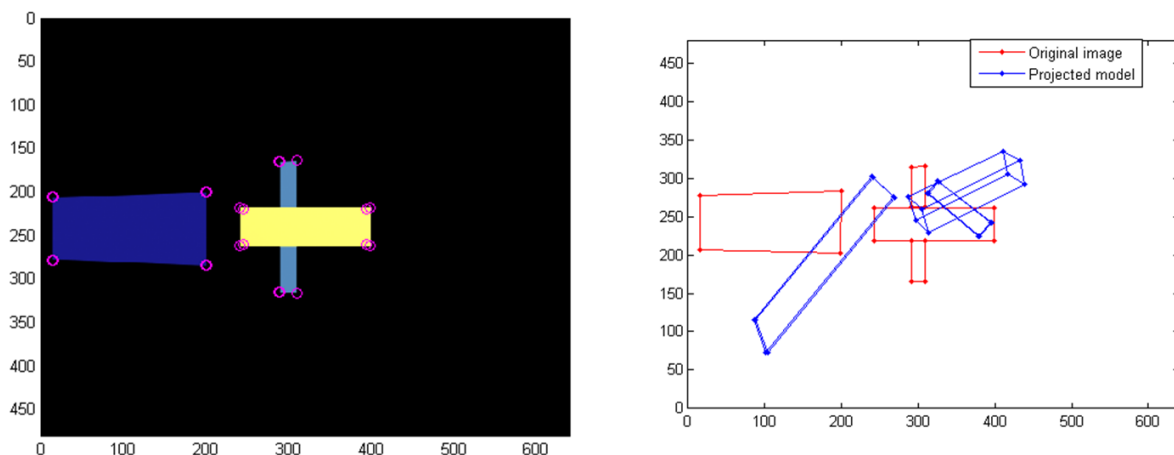


Figure 13. Left: Envisat SoftPOSIT point to image match. Purple Circle-SoftPOSIT model points. Right: Envisat SoftPOSIT initial and final pose estimation. Blue-SoftPOSIT Initial estimation. Red-SoftPOSIT Final estimation.

sequence of images from the CAD camera. The pitch axis rotation is tracked by the pose determination software.

#### IV.C. ISS Pose Estimation

Fig. 15 shows the initial position of the ISS in blue on the right side figure at  $[35;35;35]$  meters and  $[25;25;25]$  degrees, the final position is the green plot in the same figure at  $[0;0;50]$  meters and  $[0;0;0]$  degrees. The final error is  $[-0.043;-0.018;-0.005]$  meters and  $[-0.182;0.027;0.164]$  degrees. Similar to the cube and Envisat,

<sup>a</sup>orientation= $[\text{roll};\text{pitch};\text{yaw}]$  in degrees, in the pitch-yaw-roll rotation sequence

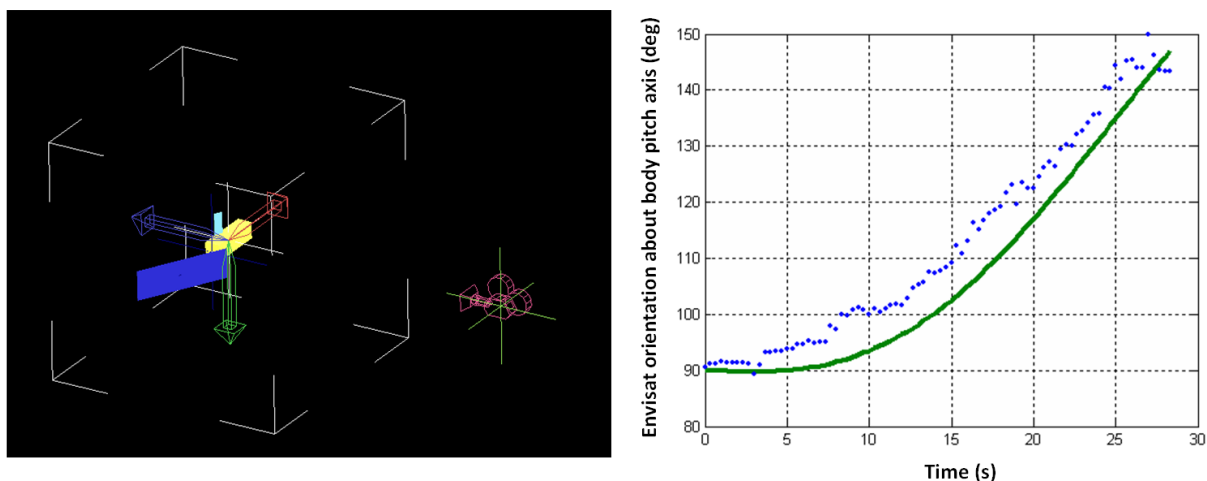


Figure 14. Left: Envisat camera scene. Right: Envisat pose estimation. Green Line-Commanded Envisat motion Blue Dots-SoftPOSIT estimation

the corner points used here is the exact case, higher error shall result when the input image is processed, these errors will depend on the lighting quality and resolution of the image. Fig. 16 shows the SoftPOSIT

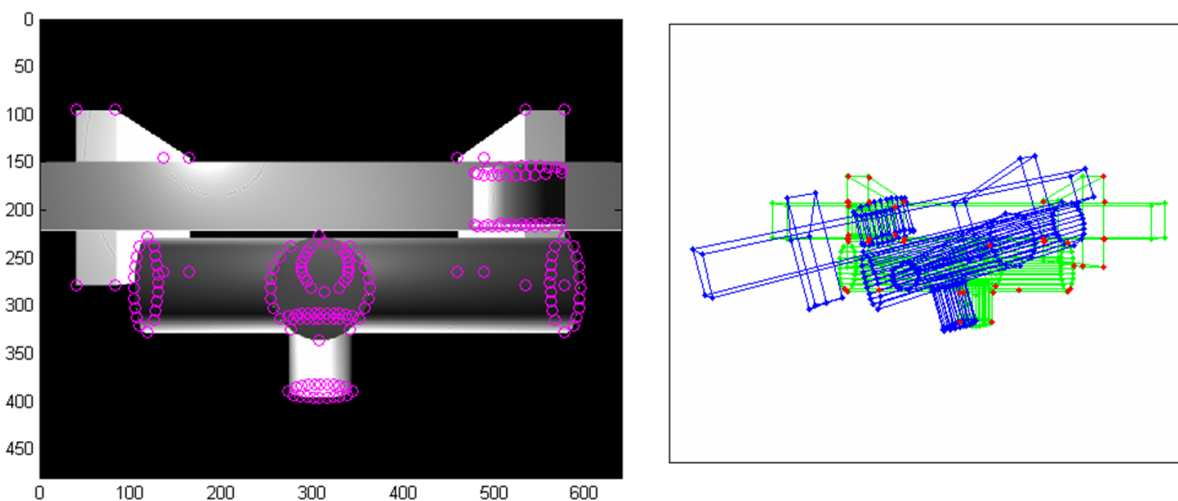


Figure 15. Left: ISS SoftPOSIT point to image match. Right: ISS SoftPOSIT initial and final pose estimation. Purple Circle-SoftPOSIT model points. Blue-Initial estimation. Green-Final estimation. Red Dots-Final SoftPOSIT model points.

calculation for a sequence of images from the CAD camera. The ISS is stationary and the camera traces a circular path around the  $z$  axis. The orientation error between the two vehicles is tracked by the pose determination software.

## Conclusion

In conclusion, the SoftPOSIT algorithm was adopted to be used for spacecraft position and orientation determination of an uncooperative target satellite. A MATLAB based software was developed to generate the internal spacecraft model, read external simulated infrared thermal image videos, produce image coordinates using Roberts Cross edge detection and Harris corner detection methods. Finally, the SoftPOSIT algorithm was used to determine the spacecraft position and pose using the internal spacecraft model and video image



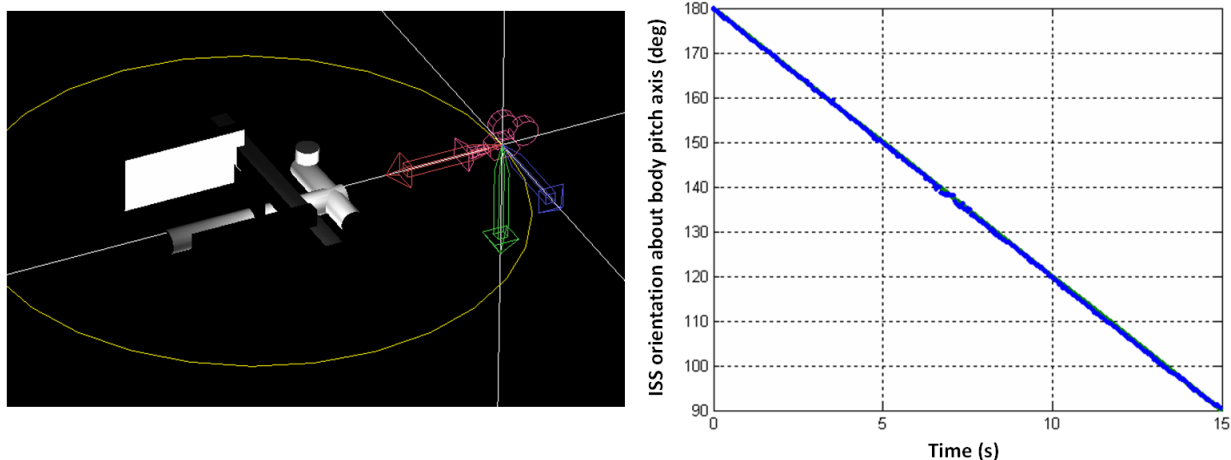


Figure 16. Left: ISS camera Scene. Right: ISS pose estimation. Green Line-Commanded Envisat motion Blue Dots-SoftPOSIT estimation

coordinates.

In the future, further development to incorporate a real infrared image for SoftPOSIT process would require robust internal model point culling, greater number of internal model edge points, to add environmental background conditions lighting effects, and robust point processing of input images.

## Acknowledgments

This research was funded by the Natural Sciences and Research Council of Canada's Engage Grant program under the award EGP #470485-14, and the Alexander Graham Bell Canada Graduate Scholarship CGSD3-453738-2014. The authors wish to acknowledge Mr. Gary Strahan and Mr. Abhishek Madaan of Infrared Camera Inc. for their support in the IR Camera software development.

## References

- <sup>1</sup>Geller, D. K., "Orbital Rendezvous: When Is Autonomy Required?" *Journal of Guidance, Control, and Dynamics*, Vol. 30, No. 4, 2007, pp. 974–981.
- <sup>2</sup>Kawano, I., Mokuno, M., Kasai, T., and Suzuki, T., "Result of Autonomous Rendezvous Docking Experiment of Engineering Test Satellite-VII," *Journal of Spacecraft and Rockets*, Vol. 38, No. 1, 2001, pp. 105–111.
- <sup>3</sup>Howard, R., Heaton, A., Pinson, R., and Carrington, C., "Orbital Express Advanced Video Guidance Sensor," *IEEE Aerospace Conference*, Piscataway, NJ, 2008.
- <sup>4</sup>ESA, "Rendezvous and Docking Technology," *ATV Information Kit*, 2008.
- <sup>5</sup>ESA, "Europe's Automated Ship Docks to the ISS," *European Space Agency News*, 2008.
- <sup>6</sup>Tweddle, B. E., *Computer Vision Based Navigation for Spacecraft Proximity Operations*, Master's thesis, Massachusetts Institute of Technology, Department of Aeronautics and Astronautics, Cambridge, MA, 2010.
- <sup>7</sup>Henshaw, C. G., Healy, L., and Roderick, S., "LIIVe: A Small, Low-Cost Autonomous Inspection Vehicle," *AIAA SPACE 2009 Conference and Exposition*, Reston, VA, 2009, AIAA Paper 2009-6544.
- <sup>8</sup>Tweddle, B. E., Saenz-Otero, A., and Miller, D. W., "Design and Development of a Visual Navigation Testbed for Spacecraft Proximity Operations," *AIAA SPACE 2009 Conference and Exposition*, Reston, VA, 2009, AIAA Paper 2009-6547.
- <sup>9</sup>Tweddle, B. E., *Computer Vision-Based Localization and Mapping of an Unknown, Uncooperative and Spinning Target for Spacecraft Proximity Operations*, Ph.D. thesis, Massachusetts Institute of Technology, Department of Aeronautics and Astronautics, Cambridge, MA, 2013.
- <sup>10</sup>Fourie, D., Tweddle, B. E., Ulrich, S., and Saenz-Otero, A., "Flight Results of Vision-Based Navigation and Control for Autonomous Spacecraft Inspection of an Unknown Object," *Journal of Spacecraft and Rockets*, Vol. 51, No. 6, 2014, pp. 2016–2026.
- <sup>11</sup>Fourie, D., Tweddle, B. E., Ulrich, S., and Saenz-Otero, A., "Vision-Based Relative Navigation and Control for Autonomous Spacecraft Inspection of an Unknown Object," *AIAA Guidance, Navigation, and Control Conference*, Reston, VA, 2013, AIAA Paper 2013-4759.
- <sup>12</sup>Tweddle, B. E., Ulrich, S., Setterfield, T., Saenz-Otero, A., and Miller, D. W., "The SPHERES-VERTIGO Goggles: An Overview of Vision-Based Navigation Research Results from the International Space Station," *12th International Symposium on Artificial Intelligence, Robotics, and Automation in Space*, Montreal, Canada, June 2014.

- <sup>13</sup>Tweddle, B. E., Setterfield, T. P., Saenz-Otero, A., Miller, D. W., and Leonard, J. J., "Experimental Evaluation of On-board, Visual Mapping of an Object Spinning in Micro-Gravity aboard the International Space Station," *IEEE/RSJ International Conference on Intelligent Robots and Systems*, Piscataway, NJ, 2014.
- <sup>14</sup>Ruel, S., Luu, T., and Berube, A., "Space Shuttle Testing of the TriDAR 3D Rendezvous and Docking Sensor," *Journal of Field Robotics*, Vol. 29, No. 4, 2012, pp. 535–553.
- <sup>15</sup>Besl, P. J. and McKay, N. D., "A Method for Registration of 3-D Shapes," *IEEE Transactions on Pattern and Machine Intelligence*, Vol. 14, No. 2, 1992, pp. 239–256.
- <sup>16</sup>Doignon, C., "An Introduction to Model-Based Pose Estimation and 3-D Tracking Technique," *Scene Reconstruction Pose Estimation and Tracking*, Bellingham WA, Rustam Stolkin (Ed.).
- <sup>17</sup>Haralick, R. M., Chu, Y. H., Watson, L. T., and Shapiro, L. G., "Matching Wire Frame Objects from their 2-D Perspective Projection," *Pattern Recognition*, Vol. 17, No. 6, 1984, pp. 607–619.
- <sup>18</sup>Lowe, D. G., "Three Dimensional Object Recognition from Single Two Dimensional Images," *Artificial Intelligence*, Vol. 31, No. 3, 1987, pp. 355–395.
- <sup>19</sup>Pinjo, Z., Cyganski, D., and Orr, J. A., "Determination of e-D Object Orientation from Projections," *Pattern Recognition Letters*, Vol. 3, 1985, pp. 351–356.
- <sup>20</sup>Thompson, D. W. and Mundy, J. L., "Three Dimensional Model Matching from an Unconstrained Viewpoint," *IEEE International Conference on Robotics and Automation*, Piscataway, NJ, 1987.
- <sup>21</sup>Gavrila, D. M. and Groen, F. C. A., "3D Object Recognition from 2D Images Using Geometric Hashing," *Pattern Recognition Letters*, Vol. 13, 1992, pp. 263–278.
- <sup>22</sup>Grimson, W. E. L. and Huttenlocher, D. P., "On the Verification of Hypothesized Matches in Model Based Recognition," *IEEE Transactions on Pattern Analysis and Machine Intelligence*, Vol. 13, No. 12, 1991, pp. 1201–1213.
- <sup>23</sup>Jurie, F., "Solution of the Simultaneous Pose and Correspondence Problem Using Gaussian Error Model," *Computer Vision and Image Understanding*, Vol. 73, No. 3, 1999, pp. 357–373.
- <sup>24</sup>David, P., DeMenthon, D., Duraiswami, R., and Samet, H., "SoftPOSIT: Simultaneous Pose and Correspondence Determination," *European Conference on Computer Vision*, Copenhagen, Denmark, 2002.
- <sup>25</sup>David, P., Dementhon, D., Duraiswami, R., and Samet, H., "SoftPOSIT: Simultaneous Pose and Correspondence Determination," *International Journal of Computer Vision*, Vol. 59, No. 3, 2004, pp. 259–289.
- <sup>26</sup>Dementhon, D. F. and Davis, L., "Model-Based Object Pose in 25 Lines of Code," *International Journal of Computer Vision*, Vol. 15, No. 1, 1995.
- <sup>27</sup>Gold, S., Rangarajan, A., Lu, C. P., Pappu, S., and Mjolsness, E., "New Algorithms for 2D and 3D Point Matching: Pose Estimation and Correspondence," *Pattern Recognition*, Vol. 31, No. 8, 1998, pp. 1019–1031.
- <sup>28</sup>Sinkhorn, R., "A Relationship Between Arbitrary Positive Matrices and Doubly Stochastic Matrices," *The Annals of Mathematical Statistics*, Vol. 35, No. 2, 1964, pp. 876–879.
- <sup>29</sup>Roberts, L., *Machine Perception of 3-D Solids*, Optical and Electro-optical Information Processing, MIT Press, 1965.
- <sup>30</sup>Canny, J., "A Computational Approach to Edge Detection," *IEEE Transactions on Pattern Analysis and Machine Intelligence*, Vol. 8, No. 6, 1986, pp. 679–698.
- <sup>31</sup>Kucharski, D., Kirchner, G., Koidl, F., C., F., Carman, R., Moore, C., Dmytrotso, A., Ploer, M., Bianco, G., Medvedskij, M., Makeyev, A., Appleby, G., Suzuki, M., Torre, J., Zhang, Z., Grunwaldt, L., and Qu, F., "Attitude and Spin Period of Space Debris Envisat Measured by Satellite Laser Ranging," *IEEE Transactions on Geoscience and Remote Sensing*, Vol. 52, No. 12, 2014, pp. 7651–7657.